

AD-A271 176

Public
gathering
collective
Davis H

ON PAGE

Form Approved
OMB NO. 0704-0188

1. AC

7/26/93

3. REPORT TYPE AND DATES COVERED

Final, 1 May 90-30 Apr 93

4. TITLE AND SUBTITLE

Synchrotron X-Ray Diffraction Analysis of Photorefractive Crystals and their Gratings.

5. FUNDING NUMBERS

DAAL03-90-G-0116

6. AUTHOR(S)

Mark Cronin-Golomb, Gerard Fogarty

7. PERFORMING ORGANIZATION NAME(S) AND ADDRESS(ES)

Electro-Optics Technology Center
Tufts University
4 Colby Street
Medford, MA 02155

DTIC
ELECTE
S OCT 21 1993
B D

8. PERFORMING ORGANIZATION REPORT NUMBER

9. SPONSORING/MONITORING AGENCY NAME(S) AND ADDRESS(ES)

U. S. Army Research Office
P. O. Box 12211
Research Triangle Park, NC 27709-2211

10. SPONSORING/MONITORING AGENCY REPORT NUMBER

ARO 27882.1-PH

11. SUPPLEMENTARY NOTES

The view, opinions and/or findings contained in this report are those of the author(s) and should not be construed as an official Department of the Army position, policy, or decision, unless so designated by other documentation.

12a. DISTRIBUTION/AVAILABILITY STATEMENT

Approved for public release; distribution unlimited.

12b. DISTRIBUTION CODE

13. ABSTRACT (Maximum 200 words)

High-resolution synchrotron x-ray diffraction imaging was used to examine the state of crystal perfection in the photorefractive ferroelectric materials barium titanate and strontium barium niobate. Ferroelectric 180 degree domains, dislocations, striations, faceted growth remnants, and other lattice features were identified. The technique was also used to image the photorefractive space charge field profile in-situ. Measurements of the field were compared with numerical simulations of the standard model of the photorefractive effect, and simulations of the x-ray image formation process.

14. SUBJECT TERMS

photorefractive crystals, synchrotron radiation, diffraction imaging, x-ray topography, photorefractive gratings.

15. NUMBER OF PAGES

38

16. PRICE CODE

17. SECURITY CLASSIFICATION OF REPORT

UNCLASSIFIED

18. SECURITY CLASSIFICATION OF THIS PAGE

UNCLASSIFIED

19. SECURITY CLASSIFICATION OF ABSTRACT

UNCLASSIFIED

20. LIMITATION OF ABSTRACT

UL

NSN 7540-01-280-5500

Standard Form 298 (Rev. 2-89)
Prescribed by ANSI Std. Z39-18
258-102

SYNCHROTRON X-RAY DIFFRACTION ANALYSIS OF
PHOTOREFRACTIVE CRYSTALS AND THEIR GRATINGS

FINAL REPORT

MARK CRONIN-GOLOMB
GERARD FOGARTY

7/26/93

U.S. ARMY RESEARCH OFFICE

DAAL03-90-G-0116

TUFTS UNIVERSITY

APPROVED FOR PUBLIC RELEASE;
DISTRIBUTION UNLIMITED

Accession For	
NTIS GRA&I	<input checked="" type="checkbox"/>
DTIC TAB	<input type="checkbox"/>
Unannounced	<input type="checkbox"/>
Justification	
By _____	
Distribution/ _____	
Availability Codes	
Distr	Avail and/or Special
A-1	

THE VIEWS, OPINIONS, AND/OR FINDINGS CONTAINED IN THIS
REPORT ARE THOSE OF THE AUTHORS AND SHOULD NOT BE
CONSTRUED AS AN DEPARTMENT OF THE ARMY POSITION, POLICY, OR
DECISION, UNLESS SO DESIGNATED BY OTHER DOCUMENTATION.

93 10 19 024

93-25001


Problem studied:

High resolution x-ray diffraction imaging was used to examine the state of crystal perfection in barium titanate and strontium barium niobate, and to probe *in-situ* the structure of the photorefractive space charge field responsible for the nonlinear optical behavior of photorefractive ferroelectric materials.

The technique of high resolution diffraction imaging uses large area, monochromatic, and well collimated beams of x-rays to form images in diffraction of lattice imperfections in a crystalline sample¹. A beam of x-rays, incident upon a crystal at the appropriate Bragg angle for the x-ray wavelength and some particular set of atomic planes, diffracts from the crystal and forms an image on the detecting medium, usually x-ray sensitive film or a video camera. In a perfect crystal, the image would be featureless, as the Bragg angle would be the same at all points of the sample. In a real sample, strains cause local variations in the Bragg angle, and hence contrast in the image. Images are formed either in Bragg geometry (reflection), or Laue geometry (transmission), as seen in figure 1. Since the local Bragg angle is dependent upon the local interplanar spacing², contrast in diffraction images is dependent only upon strain along the diffraction vector (the normal to the set of diffracting planes). With a set of diffraction images in Bragg and Laue geometries, and using symmetric (parallel to the crystal surface in reflection, or perpendicular in transmission) or asymmetric (inclined to the crystal surface) diffracting planes, it is possible to determine the actual direction and often the magnitude of the atomic displacements associated with lattice imperfections.

Summary of results:

Materials:

A total of twelve samples were examined by high resolution topography, from a variety of academic and industry sources (see table 1). The samples represent a good cross-section of what is available from the various crystal growers, and of the various surface preparation methods. This work has been greatly aided by close collaboration with the various crystal suppliers. The interest and help of Dana Anderson of the University of Colorado, John Martin of Deltronic Crystal Industries, and Mark Garrett of MIT have been particularly valuable.

The most obvious features in many of the first barium titanate diffraction images taken during this project were dense networks of surface scratches, as seen in figure 2. The typical optical quality surface polish, usually done with a diamond grit, leaves a great amount of residual surface strain, easily visible in high-resolution diffraction imaging, which can obscure other important structure within the crystal.. The skill of the crystal

! polishers has increased dramatically, and with the use of sub-micron particle size colloidal silica polishing compounds, excellent quality surfaces are now routine (figure 3). In particular, Dana Anderson of the University of Colorado, and Deltronic Crystal Industries both have demonstrated the ability to consistently deliver high quality surfaces on barium titanate, without depoling the samples in the process.

The well polished samples show remarkable short and long range lattice regularity. The entire crystal usually diffracts at once, as can be seen in figures 2, 3, and 4, and rocking curve widths are on the order of only a few tens of arc seconds. Lattice warping and variation in the lattice constant are minimal (a few arc seconds) over the typical sample surface area of 25 mm^2 , and are likely not significant.

While the lattice is quite regular, ferroelectric domains are often seen. The most easily visible of these are the 90 degree ferroelectric domains, as in the top left hand corner of figure 2. These domains, which also are visible optically, can be completely removed by poling, and hence usually are absent from well-poled samples.

Anti-parallel or 180 degree ferroelectric domains are also visible in certain diffraction images (see figures 4 and 5). These domains are visible only in images where a component of the diffraction vector is along the [001] or c-axis. Since barium titanate lacks a center of symmetry, the x-ray structure factors for $(a,b,1)$ and $(\bar{a},\bar{b},\bar{1})$ diffractions are not the same, and this leads to a slightly different coupling between the two diffracted wavefields inside the crystal for the bulk and domain regions. This coupling difference results in a slight contrast change in the image. We believe this is the first instance of non-destructive imaging of anti-parallel domain patterns within the volume of a ferroelectric crystal, and a non-ambiguous method of assessing the degree of poling in a given crystal.

The 180 degree domains have been observed in every crystal, indicating that no samples were perfectly poled, although the vast majority of each sample's volume was free of domains. The images of domains are usually shaped like needles or tweezers (see figure 5), [001] oriented, and clustered near the faces and c-edges of the samples. The pendellosung effect (a dynamical x-ray diffraction effect in which the diffracted intensity is a periodic function of sample thickness³) is also observed in transmission images of domains in the interior of the samples, as fringes covering equal-thickness portions of the cone-shaped domains. (see figure 5)

Non [001] oriented anti-parallel domain walls are also possible in certain circumstances, as seen in figure 6. This sample was accidentally depoled by cooling through the tetragonal-orhtorhombic phase transition, and subsequently mechanically poled to remove the 90 degree domains. After electrical poling, the few remaining domains were [001] oriented (figure 7).

The identification of the domains was confirmed by an experiment in which an electric field of 360 V/cm was applied to the crystal at room temperature, alternately parallel and anti-parallel to the c-axis. As expected, the field anti-parallel to the c-axis caused the domain regions to grow (figure 8), and the opposite field (along the c-axis) caused the domain regions to shrink again (figure 9). Due to the low temperature, a large amount of hysteresis was observed: some domains were induced which could only be removed by high temperature poling.

Apart from domains, there also were other deviations from perfection observed in some samples. Most prominent among these were dislocations, primarily edge (figure 4) and screw (figure 10), although a few other unidentified dislocations also were observed. Since the density of the dislocations was too low to be a source of the optical scattering responsible for seeding fanning, it is now believed that the size of the scatterers responsible for the fanning lies below the micron scale resolution limit of the nuclear emulsion plates used to record the diffraction images.

Some other interesting image features have been evidence of faceted growth and facet competition, as seen in figure 11. A closeup of this image (figure 12) reveals a periodically wandering boundary between the facets. During crystal growth, each of these facets would alternately grow faster than its neighbor (perhaps due to thermal or mechanical asymmetry in the melt), periodically altering the slope of the interface between them, and also causing striations. Similar behavior has been observed previously in BSO.⁴ The striations are also visible in other crystals in which faceted growth is not seen (figure 10), but the lack of faceting is likely due simply to the manner in which the samples were cut out of the boule. Partial facet interfaces appear as low angle grain boundaries in nearly all the samples examined.

Two samples of SBN were also briefly examined. The first, provided by Nikolai Bogodaev of the Institute of Physics, Russian Academy of Science, showed a very large number of surface scratches, and drastic lattice warping (see figure 13). The sample was grown using an unconventional technique in which the boule is not rotated as pulled from the melt, and it is not yet known if lattice warping is typical of such growth.

The other sample, grown by Deltronic Crystal Industries, showed some growth effects similar to those seen in barium titanate (figure 14), but with unusually shaped interfaces. The long range lattice regularity of SBN is quite remarkable, given that the material is a solid solution, and not stoichiometric. This lattice regularity is encouraging for future diffraction imaging of SBN.

A sample of a $.5\mu\text{m}$ thin film of BGO on a sapphire substrate provided by Arun Inam of Bellcore also was examined, as seen in figure 15. The film showed a cellular

structure and numerous non-diffracting regions, as well as an exceptionally broad rocking curve (0.2 degrees), indicative of a high degree of disorder. A more extensive survey is needed to determine the various lattice irregularities present and their effect upon the optical properties of the films, but these first imaging results are encouraging.

Photorefractive gratings:

After the forementioned experiments demonstrated the ability of high resolution topography to reveal small deviations from lattice perfection in barium titanate, the technique was used to observe photorefractive gratings in-situ. Two nearly equal amplitude beams split from a 50 milliwatt frequency doubled YAG laser were used to write a photorefractive grating in a barium titanate sample (figures 16a and b). The space charge field responsible for the photorefractive index grating also produces a periodic lattice strain via the piezoelectric effect, which is visible in x-ray diffraction images.

Gratings with period ranging from 7 to 70 microns, and with various orientations relative to the c-axis, have been imaged. Transmission images are visually striking (figure 17), and are sensitive to small amounts of induced lattice strain, but integration through the volume of the crystal by diffraction makes interpretation of the images difficult. Reflection images are more useful for analytical purposes because they sample a smaller volume of the crystal. Similarly, gratings aligned along the c-axis induce smaller lattice distortions than those oriented at an angle to the c-axis (due to the structure of the piezoelectric tensor of barium titanate), but allow easier recovery of the induced strain magnitude and hence electric field magnitude.

Figure 18 shows an interesting reflection image of a 50 μm period grating. There is a clear spatial phase shift of the grating as it crosses the 180 degree domain boundary, caused by the reversal of sign of the c-axis with respect to the space charge field. This shift simultaneously confirms that the needle shaped features are 180 degree domains, and that the grating indeed is caused by the photorefractive effect.

The grating images themselves were recorded both with a 20 μm resolution CCD camera, and with 1 μm resolution nuclear emulsion plates. Since the high spatial resolution of the plates was necessary for analysis of the gratings, the plates were digitized at 1 μm resolution using the microscopy facilities at the University of Massachusetts Medical School Center for Molecular Medicine, and image processing techniques were used to recover the structure of the photorefractive gratings.

Multiple images of the same grating at selected points on the rocking curve were used to calibrate the film response, and the measured rocking curve and published values of the piezoelectric constants⁵ used to calculate electric field profiles and magnitudes. One such field profile is shown in figure 19. This looks quite similar to what is expected from numerical solution of the Kukhtarev model of grating formation⁶ (see figure 20), however the amplitude of the electric field is quite a bit higher. Additionally, there are high frequency components present in the data not predicted by the model. These higher

frequencies may be irregularities in the light interference pattern forming the grating, or could have another explanation, perhaps rooted in the physics of the dynamical diffraction of x-rays, which we are currently studying.

An image of nominally the same grating was also taken in symmetric reflection. As can be seen in figure 21, the grating appears quite different from the one of figure 19. The higher frequency components are absent, and the shape is quite different. In addition, the amplitude is much higher than the 160 V/cm predicted by the Kukhtarev model (figure 20).

Due to the differences between the symmetric and asymmetric images, it appears likely that dynamical x-ray diffraction effects are causing differences between the observed shapes and magnitudes of the gratings, and the shapes and magnitudes expected. Some simulations of x-ray diffraction⁷ in a crystal with grating induced distortion were performed, in order to obtain a more quantitative picture of the distortions introduced into the grating image by the image formation process.

Figure 22 shows a simulation of the effects of progressively higher amounts of grating lattice distortion on a symmetric surface x-ray diffraction image of a simple sinusoidal grating. Particularly in the higher strain cases, the image can be quite distorted relative to the actual grating shape. The exact magnitude of the linear absorption coefficient chosen for the simulation has a large bearing on the exact shape of the grating: lowering the absorption coefficient from the value used in producing figure 22 results in additional higher frequency components being introduced into the image, similar to those noted experimentally in figure 19. Quantitatively meaningful results will depend upon realistic values for the linear absorption, and x-ray structure factors for the particular diffractions involved. Simulations of asymmetric diffraction appear to show substantially less distortion of the grating shape than in symmetric diffraction, implying that the experimental results from asymmetric diffraction as they stand are probably closer to the truth. It should be possible to correct for the diffraction effects and obtain more accurate grating profiles from both the symmetric and asymmetric diffraction images, given realistic values for the appropriate crystal parameters.

Images of fanning were also successfully obtained, as can be seen in figure 23. There is interesting structure in this image even at the 1 micron level, and improvement of the spatial resolution below that would likely yield a wealth of information on the grating structures associated with fanning. This data would greatly help current work on beam propagation method simulations of photorefractive devices⁸.

Conclusions:

In general, the quality of the barium titanate samples examined could be termed excellent from a crystallographic point of view. None of the defects seen appear in sufficient numbers to be possible sources of fanning, so the size of the defects is believed to be below 1 micron. Improvements in the spatial resolution of diffraction imaging would allow a search for such defects, although it is not yet clear what the fundamental resolution limits are.

Anti-parallel ferroelectric domain patterns were imaged non-destructively for the first time. These domains appeared in every sample examined, indicating incomplete, but usually quite good, poling. The reasons for incomplete poling are still unclear.

Measurements of photorefractive gratings *in-situ* were made for the first time. The spatial profile of the space charge field was recovered, and explanations for differences with the theory have been proposed. The best measurements agree reasonably well with the standard model with the exception of the as yet unexplained discrepancy between the theoretical and experimental electric field magnitudes. The results demonstrate the possibility of imaging of devices (i.e. self-pumped phase conjugate mirrors) in operation.

Figures and Tables

Table 1: Summary of samples studied.

Figure 1: Schematic representation of diffraction imaging geometry.

Figure 2: (224) diffraction image of crystal 188E in Bragg geometry (reflection) at 10 keV. Randomly oriented linear features are surface scratches. The displaced triangular area in the upper left corner is a 90 degree domain.

Figure 3: (600) diffraction image of crystal BTUC2 in Bragg geometry at 12 keV, showing excellent lattice regularity and surface polish.

Figure 4: (002) diffraction image of crystal BTUC2 in Laue geometry (transmission) at 12keV. The linear features running horizontally are edge dislocations, and needle or spike like features running vertically are 180 degree domains.

Figure 5: Close up of figure 4, showing 180 dgree domain shape and fringes due to the pendellosung effect.

Figure 6: (002) diffraction image of crystal F18W1 in Laue geometry at 12keV, showing non-crystallographically oriented 180 degree domain walls.

Figure 7: (002) diffraction image of crystal F18W1 in Laue geometry at 12keV after repoling, showing a few crystallographically oriented domains. The large crack at the upper left was accidentally introduced while poling.

Figure 8: (402) diffraction image of crystal BTUC2 in Bragg geometry at 12keV, showing growth of domains after 360 V/cm electric field was applied anti-parallel to the c-axis.

Figure 9: (402) diffraction image of crystal BTUC2 in Bragg geometry at 12keV, showing shrinkage of domains after application of 360 V/cm electric field parallel to c-axis.

Figure 10: (020) diffraction image of crystal BTUC2 in Laue geometry at 12keV, showing growth striations, and screw dislocations running horizontally.

Figure 11: (400) diffraction image of crystal 20F18-2 in Bragg geometry at 10keV, showing growth faceting, facet competition, and growth striations.

Figure 12: Closeup of figure 11.

Figure 13: (800) diffraction image of SBN sample SBNSU1 in Bragg geometry at 8keV, showing surface scratches and lattice warping.

Figure 14: (004) diffraction image of SBN sample SBND1 in Bragg geometry at 8keV, showing growth striations, and odd facet shapes.

Figure 15: (444) diffraction image of BSO film in Bragg geometry at 10keV, showing cellular structure.

Figure 16a: Schematic of the apparatus used to write photorefractive gratings on beamline X23A3 at the National Synchrotron Light Source. The beam from the laser is split, and the two resulting beams are interfered at the crystal to produce the grating. The complicated beam path is to achieve a small angle between the beams necessary for long period ($>50\mu\text{m}$) gratings. The entire assembly rotates as a unit to allow changes in Bragg angle without altering the grating.

Figure 16b: Photograph of the apparatus used to write photorefractive gratings on beamline X23A3 at the National Synchrotron Light source. The sample is near the center of the photo, where the beams intersect.

Figure 17: (002) diffraction image of sample F18W1 in Laue geometry at 12 keV, with 40 micron period photorefractive grating.

Figure 18: (402) diffraction image of sample F18W1 in Bragg geometry at 12 keV, with 40 micron grating, showing grating phase shift at ferroelectric domain boundaries.

Figure 19: Photorefractive space charge field calculated from (402) Bragg geometry rocking curve sequence at 12keV.

Figure 20: Simulation of the expected space charge field of 40 micron period grating in barium titanate.

Figure 21: Photorefractive space charge field calculated from (400) Bragg geometry rocking curve sequence at 12keV.

Figure 22: X-ray diffraction simulation of the diffraction image produced by a crystal with a sinusoidal grating. Successive curves represent progressively higher amplitudes of the induced sinusoidal strain, with the largest amplitude curve representing approximately the amount of strain corresponding to the grating of figure 21.

Figure 23: (002) diffraction image of sample F18W1 in Laue geometry at 12keV, showing fanning grating structure. Laser beam enters from the bottom edge of the crystal.

References

- 1 B. Steiner et al., *Prog. Crystal Growth and Charact.*, **20**, 189 (1990).
- 2 C. Kittell, *Solid State Physics*, Wiley, 1986.
- 3 B. W. Batterman et al., *Rev. Modern Physics*, **36**, 681 (1964).
- 4 B. Steiner et al., *Jrnl. Crystal Growth*, **87**, 79 (1988).
- 5 A. Schaefer et al., *Ferroelectrics*, **69**, 253 (1986).
- 6 N. V. Kukhtarev et al., *Ferroelectrics*, **22**, 949 (1979).
- 7 J. Gronkowski, *Physics Reports*, **206** (1991).
- 8 M. Cronin-Golomb, *Optics Comm.*, **89**, 276 (1992).

Publications

"Synchrotron X-ray Diffraction Imaging of Photorefractive Crystals", G. Fogarty, M. Cronin-Golomb, B. Steiner, *OSA topical meeting on Photorefractive Materials, Effects, and Devices*, July 1991.

"High Resolution X-ray Diffraction Imaging of Photorefractive Gratings in Barium Titanate", G. Fogarty, M. Cronin-Golomb, B. Steiner, U. Laor, CLEO 93.

"X-ray Diffraction Imaging of Photorefractive Crystals", G. Fogarty, M. Cronin-Golomb, B. Steiner, R. Dobbins, 1991 NSLS users meeting.

"Direct Observation of Optically Induced Gratings by High Resolution Diffraction Imaging", G. Fogarty, M. Cronin-Golomb, U. Laor, B. Steiner, 1992 NSLS users meeting.

"High Resolution Diffraction Imaging of Photorefractive Gratings", G. Fogarty, M. Cronin-Golomb, B. Steiner, *Synchrotron Radiation News* 6.4, 11 (1993).

"High Resolution Diffraction Imaging of Photorefractive Gratings", G. Fogarty, M. Cronin-Golomb, B. Steiner, U. Laor 1993 NSLS users meeting.

Participating Personnel

Direct Participants:

Mark Cronin-Golomb
Tufts University

Gerard Fogarty *
Tufts University

Bruce Steiner
National Institute of Standards and Technology

Uri Laor
National Institute of Standards and Technology, Nuclear Research Centre, Negev, Israel.

Ronald Dobbyn
National Institute of Standards and Technology

Collaborators:

Mark Garrett
Massachusetts Institute of Technology
(Presently with Sandoz Optoelectronique)

John Martin
Deltronic Crystal Industries

Dana Anderson
University of Colorado, Boulder

Tom Pollack
Sanders Associates

Barry Wechsler
Hughes Research Lab

Nikolai Bogodaev
Institute of Physics, Russian Academy of Science

Arun Inam
Bellcore

* this work forms the basis of a PhD thesis

Table 1
Sample Summary

Crystal	Designation	Material	Supplier	Grower	Polish	Remarks
BTUC1		BT	DZA	Sanders	DZA, DCI	excellent polish
BTUC2		BT	DZA	Sanders	DZA	excellent polish, 180 degree domains, dislocations, striations
F18-W1		BT	DCI	DCI	DCI	excellent polish, photorefractive gratings
20F 18-1		BT	MHG	MHG	MHG	surface scratches, faceted growth, 180 degree domains, striations
20F 18-2		BT	MHG	MHG	MHG	surface scratches, faceted growth, 180 degree domains, striations
188E		BT	Sanders	Sanders	Sanders	surface scratches
186C2		BT	Sanders	Sanders	Sanders	surface scratches
224B		BT	Sanders	Sanders	Sanders	surface scratches
218C		BT	Sanders	Sanders	DZA	excellent polish, 180 degree domains
BT78		BT	Hughes	Hughes	Hughes	surface scratches, domains
BT62		BT	Hughes	Hughes	Hughes	surface scratches, domains
BTCO		BT	Hughes	Hughes	Hughes	surface scratches, domains
SBN		SBN	NB	NB	NB	surface scratches, domains
SBN		SBN	DCI	DCI	DCI	growth rings
SBNDC1		BGO	AI	AI	---	cellular structure
BCO-1						

BT barium titanate

SBN strontium barium niobate

DZA Dana Z. Anderson, University of Colorado

MHG Mark H. Garrett, MIT

Nikolai Bogodaev, Institute of Physics, Russian Academy of Science

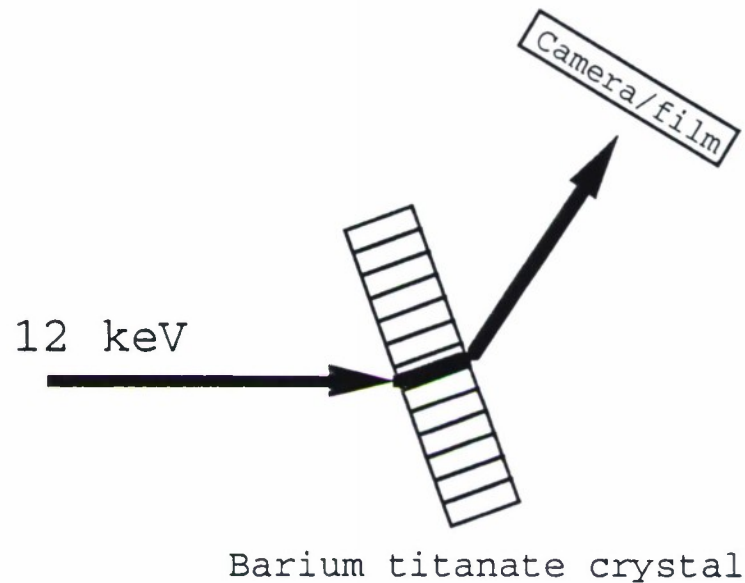
AI Arun Inam, Bellcore

DCI Deltronic Crystal Industries

Sanders Associates

Hughes Research Lab

Laue Geometry (Transmission)



Bragg Geometry (Reflection)



Figure 1: Schematic representation of diffraction imaging geometry.

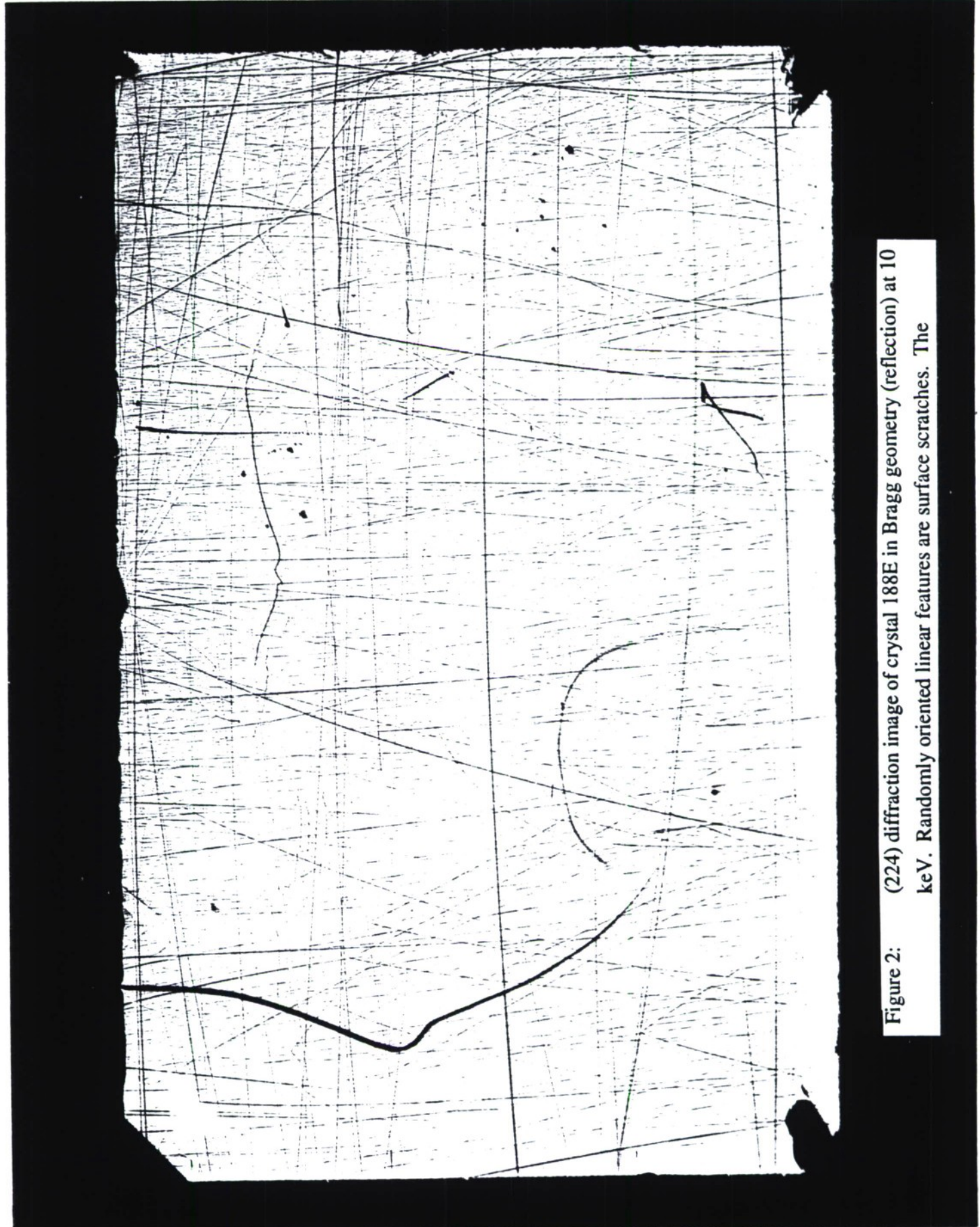


Figure 2: (224) diffraction image of crystal 188E in Bragg geometry (reflection) at 10 keV. Randomly oriented linear features are surface scratches. The

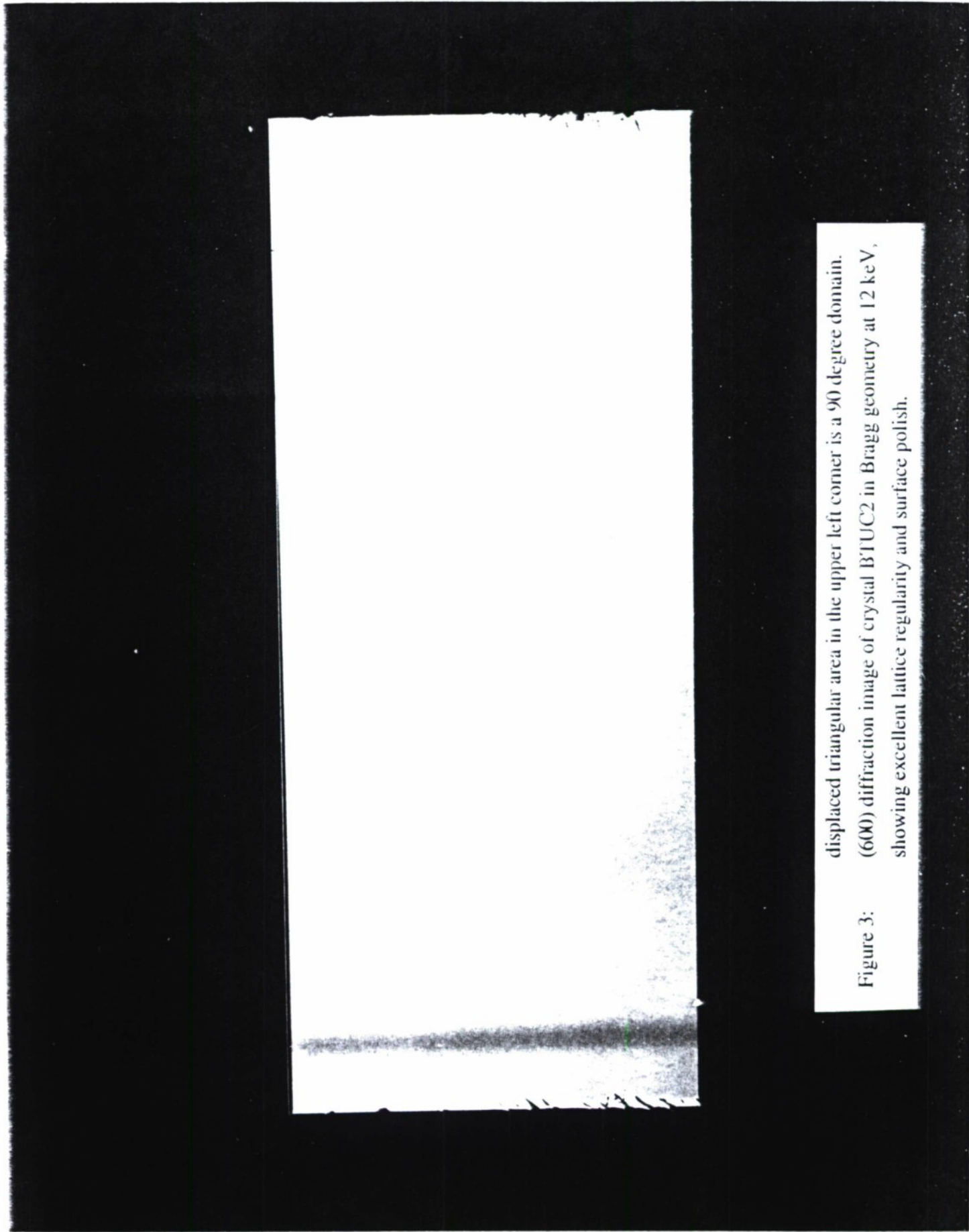


Figure 3: (600) diffraction image of crystal BTUC2 in Bragg geometry at 12 keV, showing excellent lattice regularity and surface polish.

displaced triangular area in the upper left corner is a 90 degree domain.

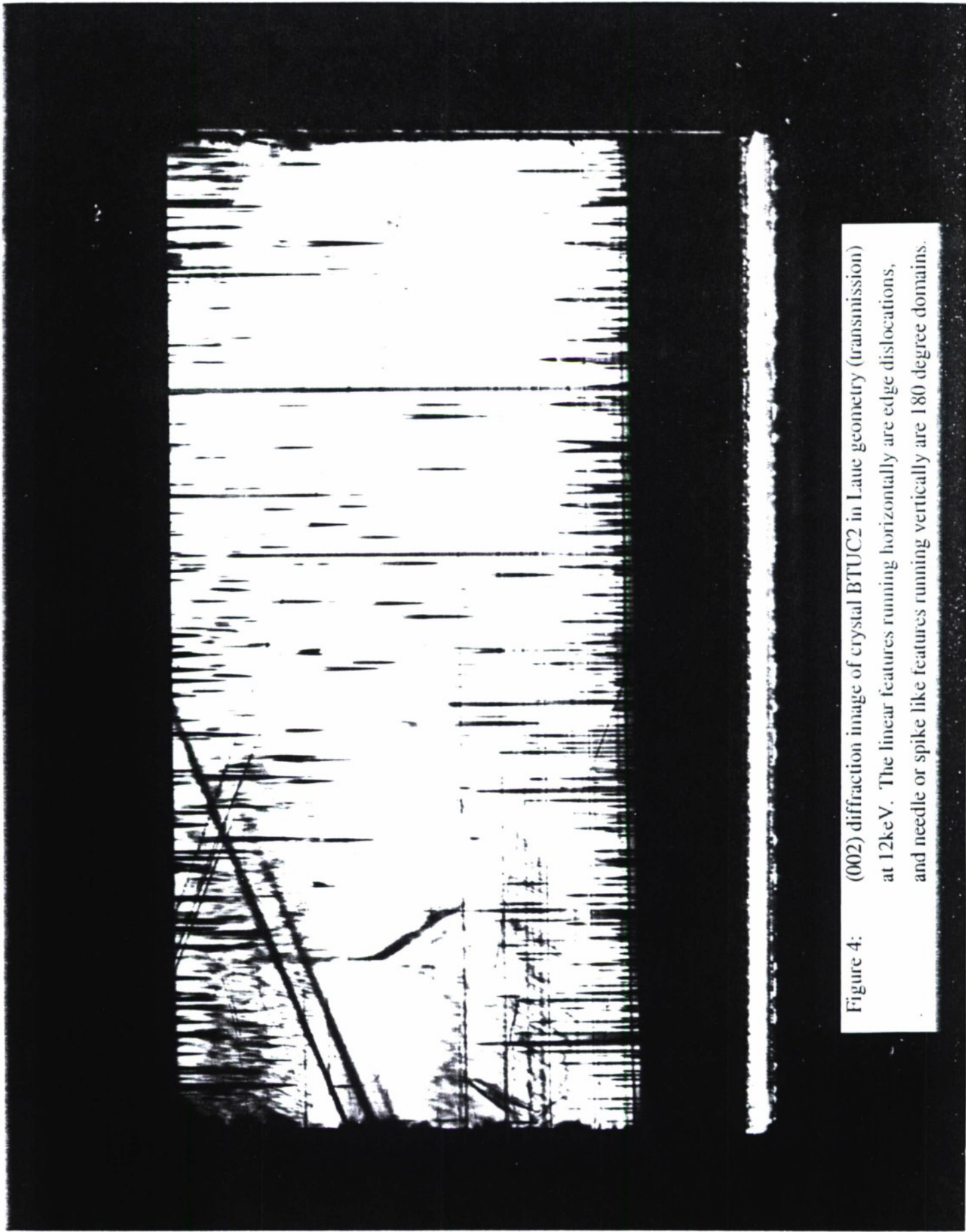


Figure 4: (002) diffraction image of crystal BTUC2 in Laue geometry (transmission) at 12keV. The linear features running horizontally are edge dislocations, and needle or spike like features running vertically are 180 degree domains.

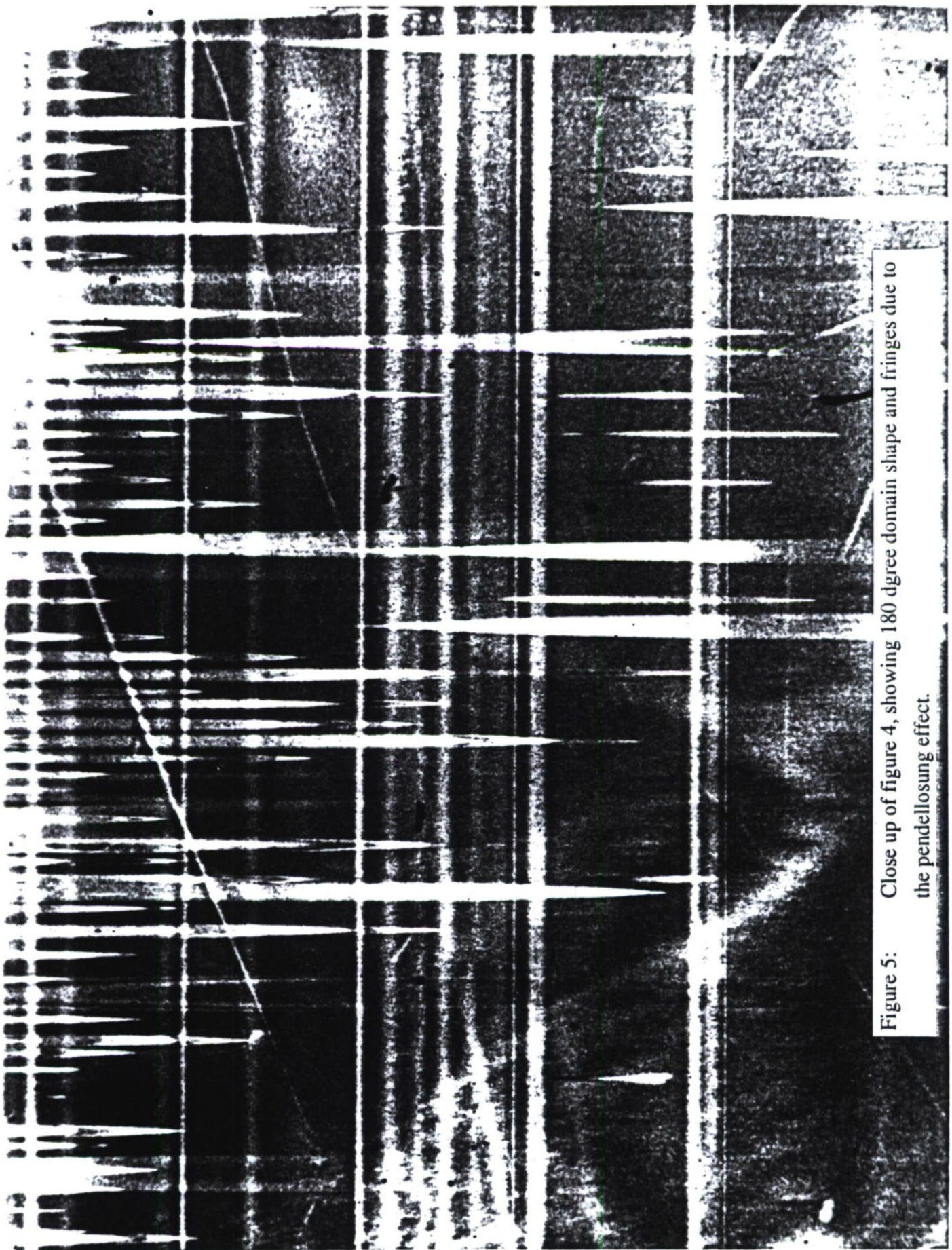


Figure 5: Close up of figure 4, showing 180 degree domain shape and fringes due to the pendelosung effect.

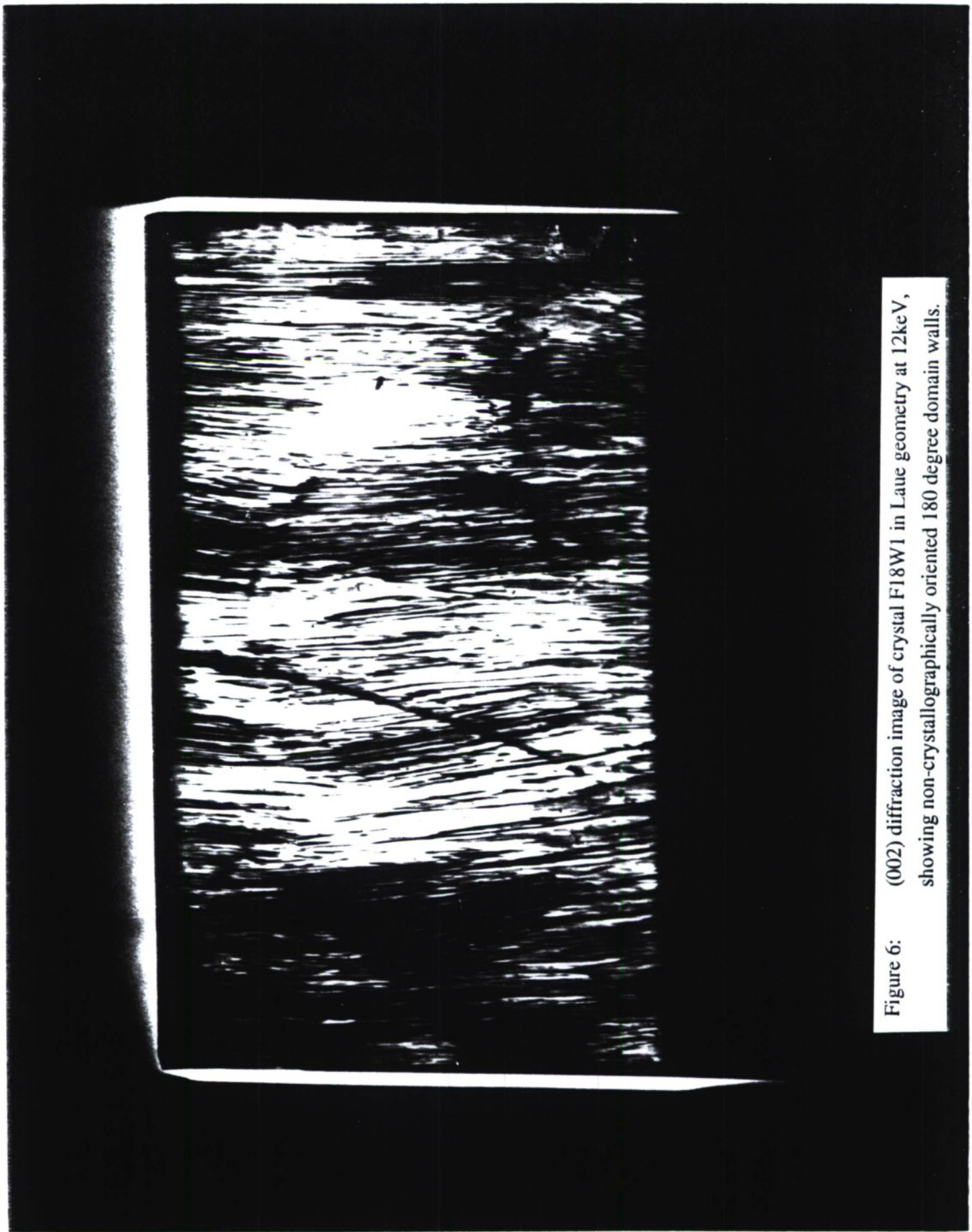


Figure 6: (002) diffraction image of crystal F18W1 in Laue geometry at 12keV, showing non-cryystallographically oriented 180 degree domain walls.



Figure 7: (002) diffraction image of crystal F18W1 in Laue geometry at 12keV after repoling, showing a few crystallographically oriented domains. The large crack at the upper left was accidentally introduced while poling.

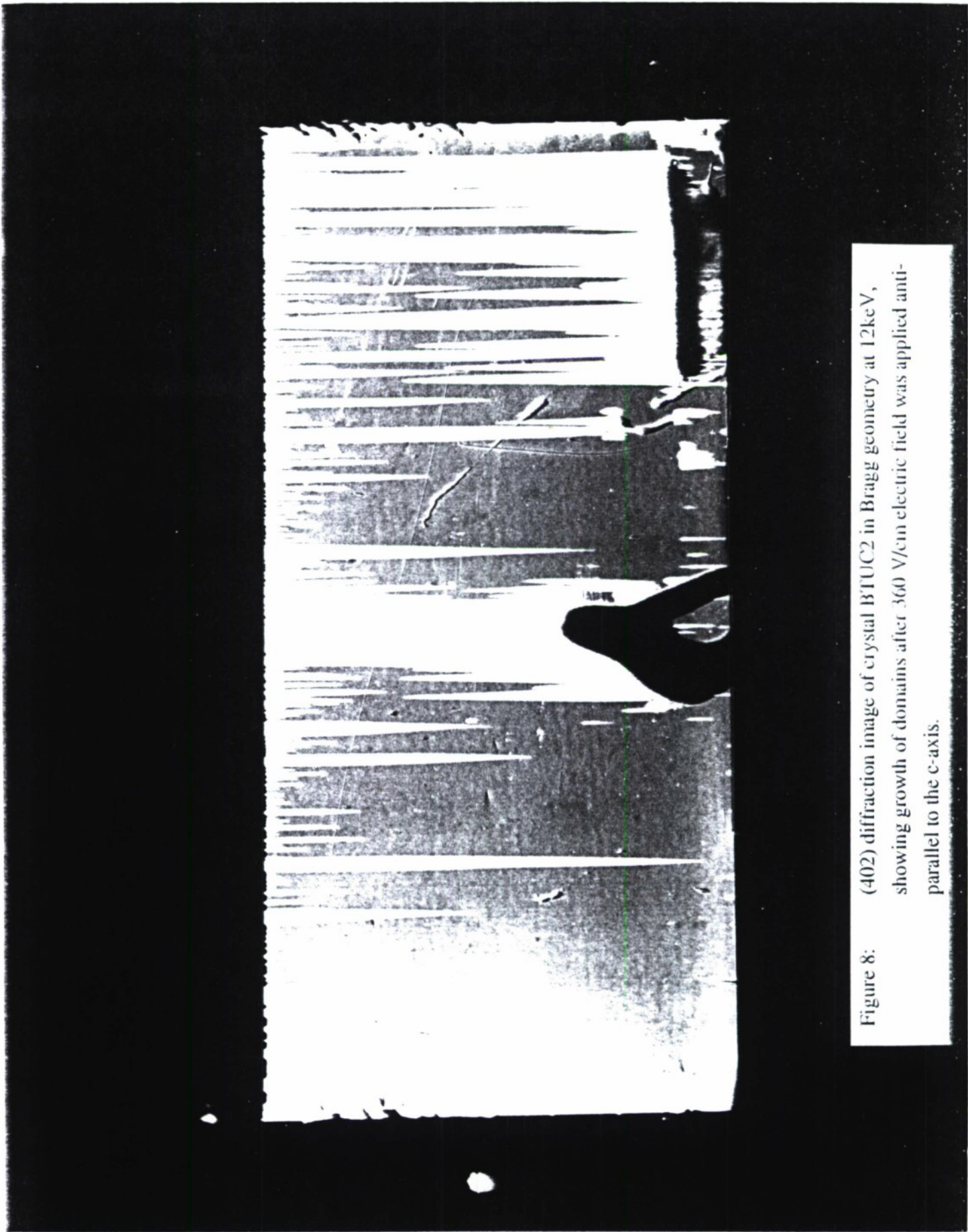


Figure 8: (402) diffraction image of crystal BTUC2 in Bragg geometry at 12 keV, showing growth of domains after 360 V/cm electric field was applied anti-parallel to the c-axis.

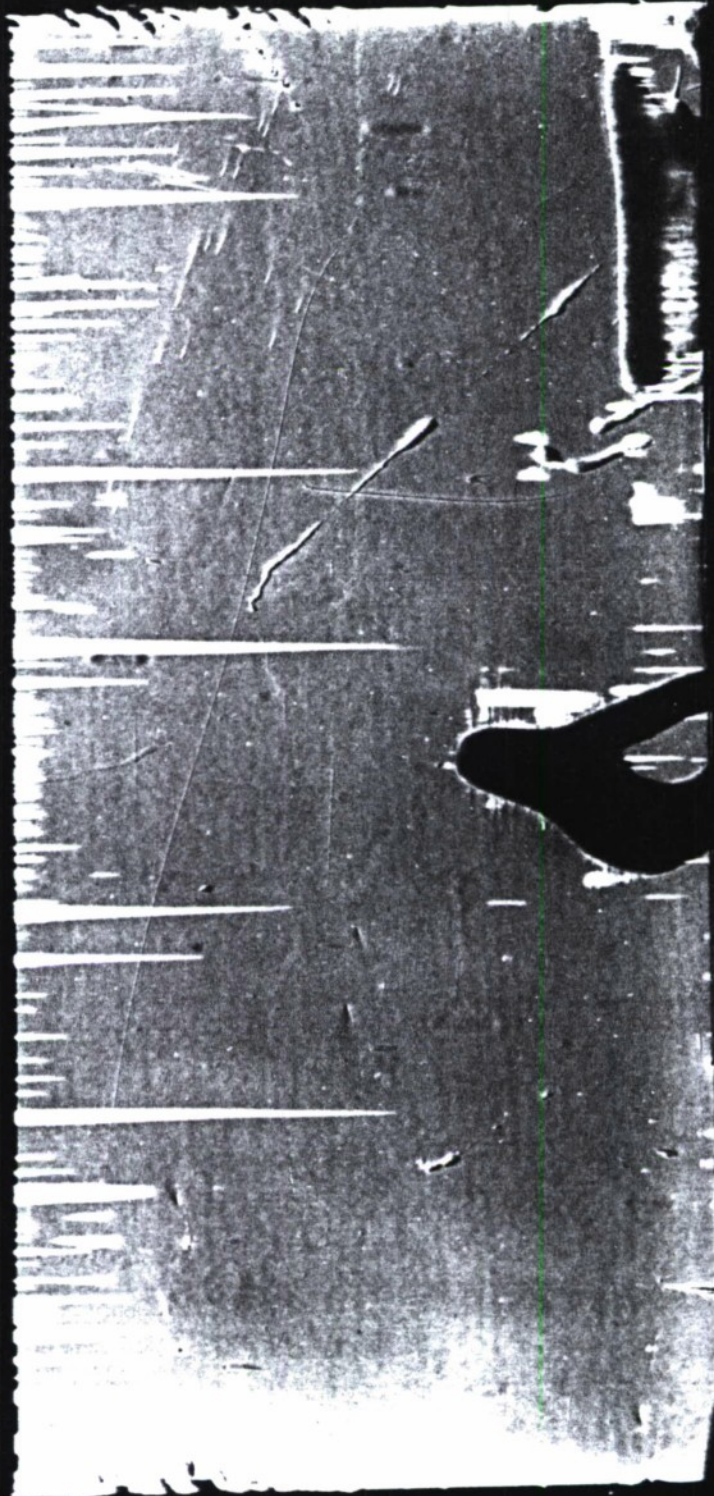


Figure 9: (402) diffraction image of crystal BTUC2 in Bragg geometry at 12keV, showing shrinkage of domains after application of 360 V/cm electric field parallel to c-axis.

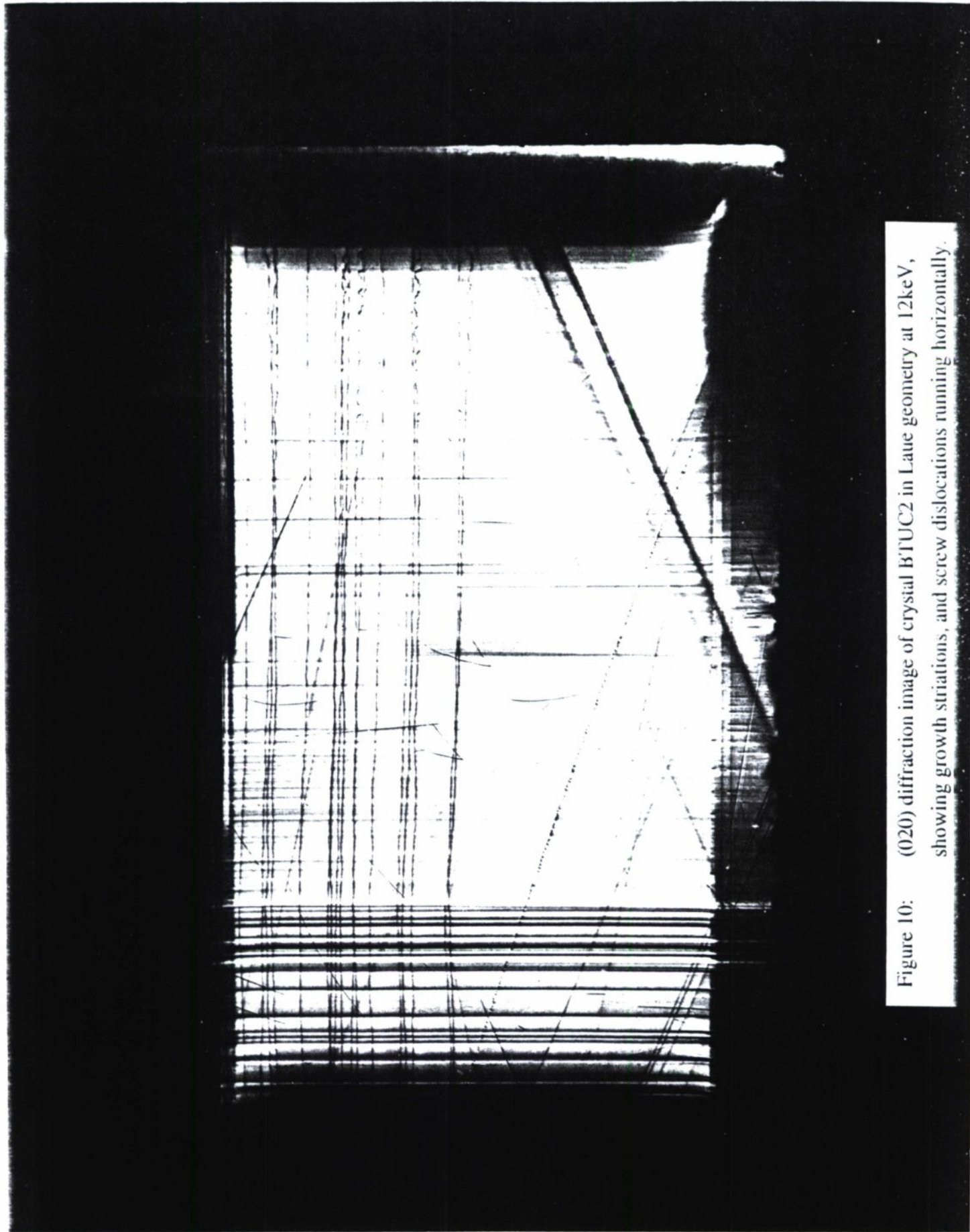


Figure 10: (020) diffraction image of crystal BTUC2 in Laue geometry at 12keV, showing growth striations, and screw dislocations running horizontally.

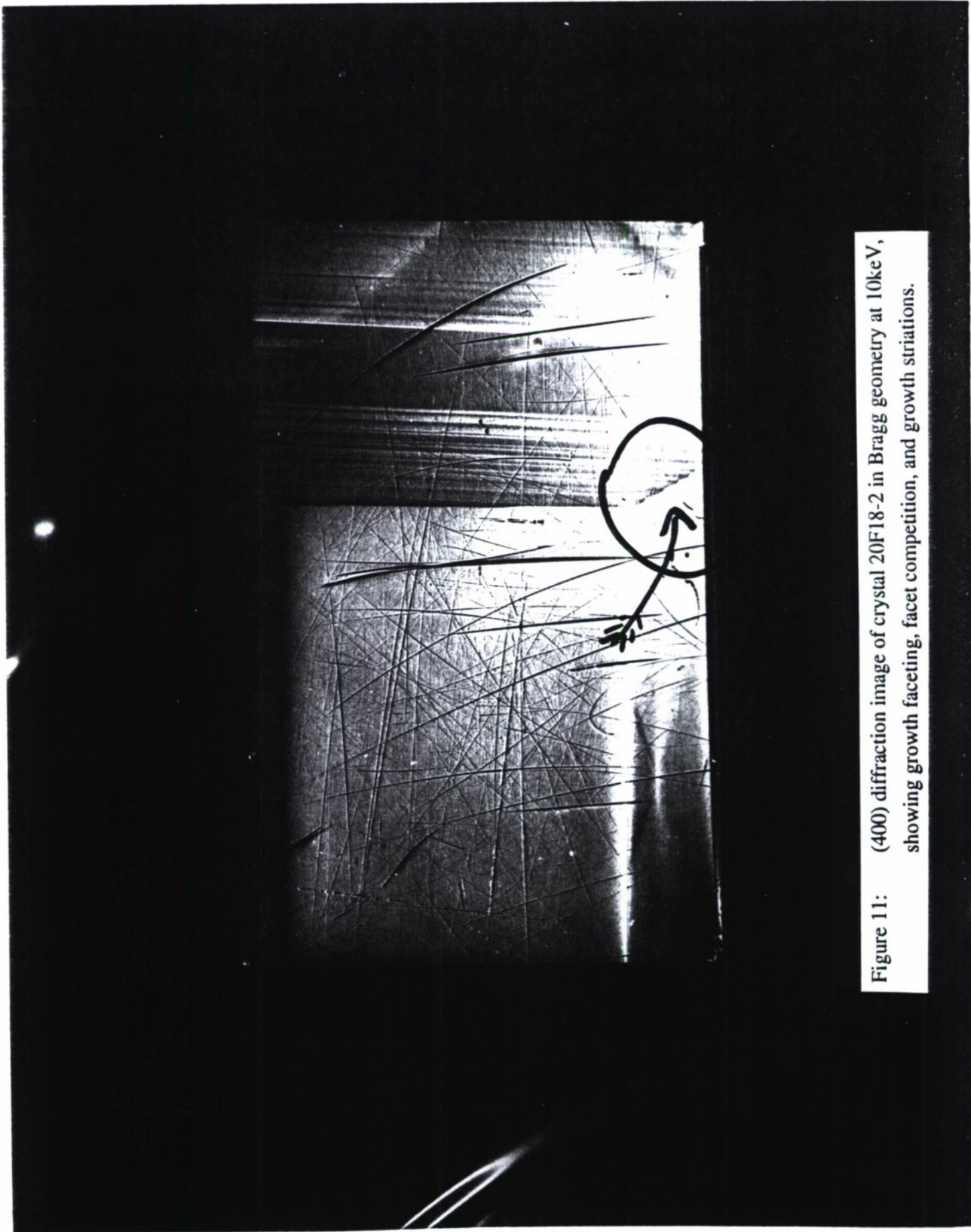


Figure 11: (400) diffraction image of crystal 20F18-2 in Bragg geometry at 10keV, showing growth faceting, facet competition, and growth striations.

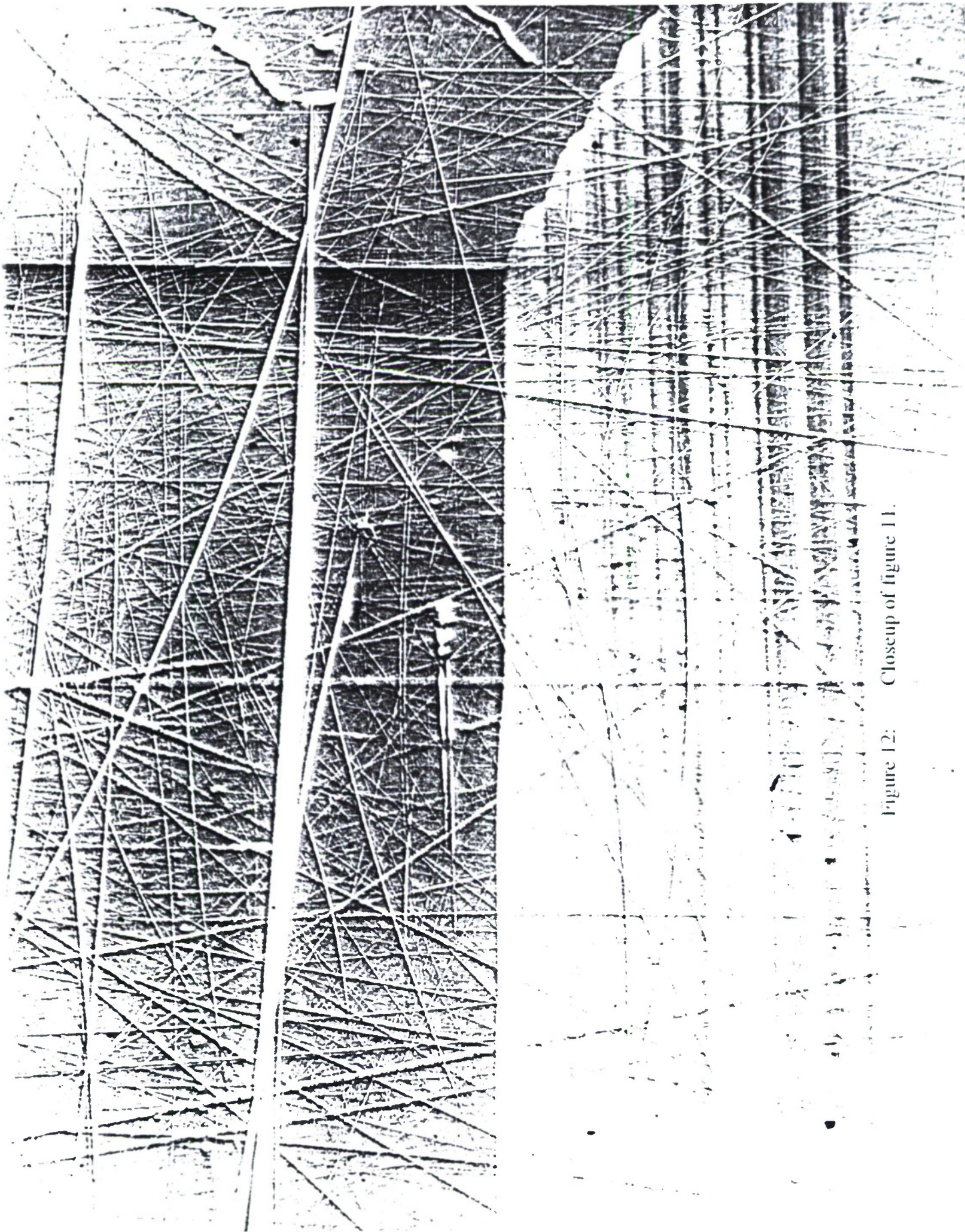


Figure 12: Closeup of figure 11.

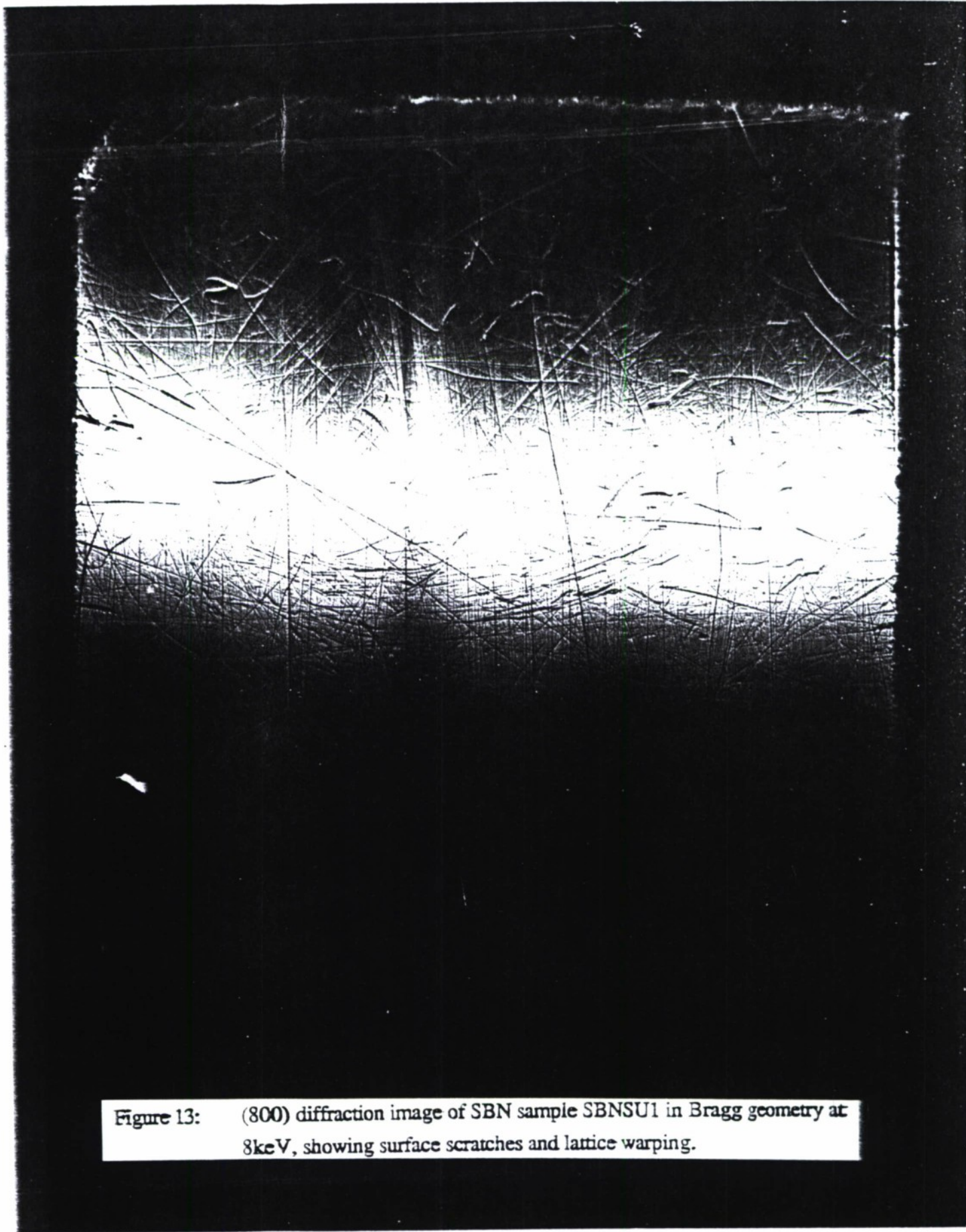
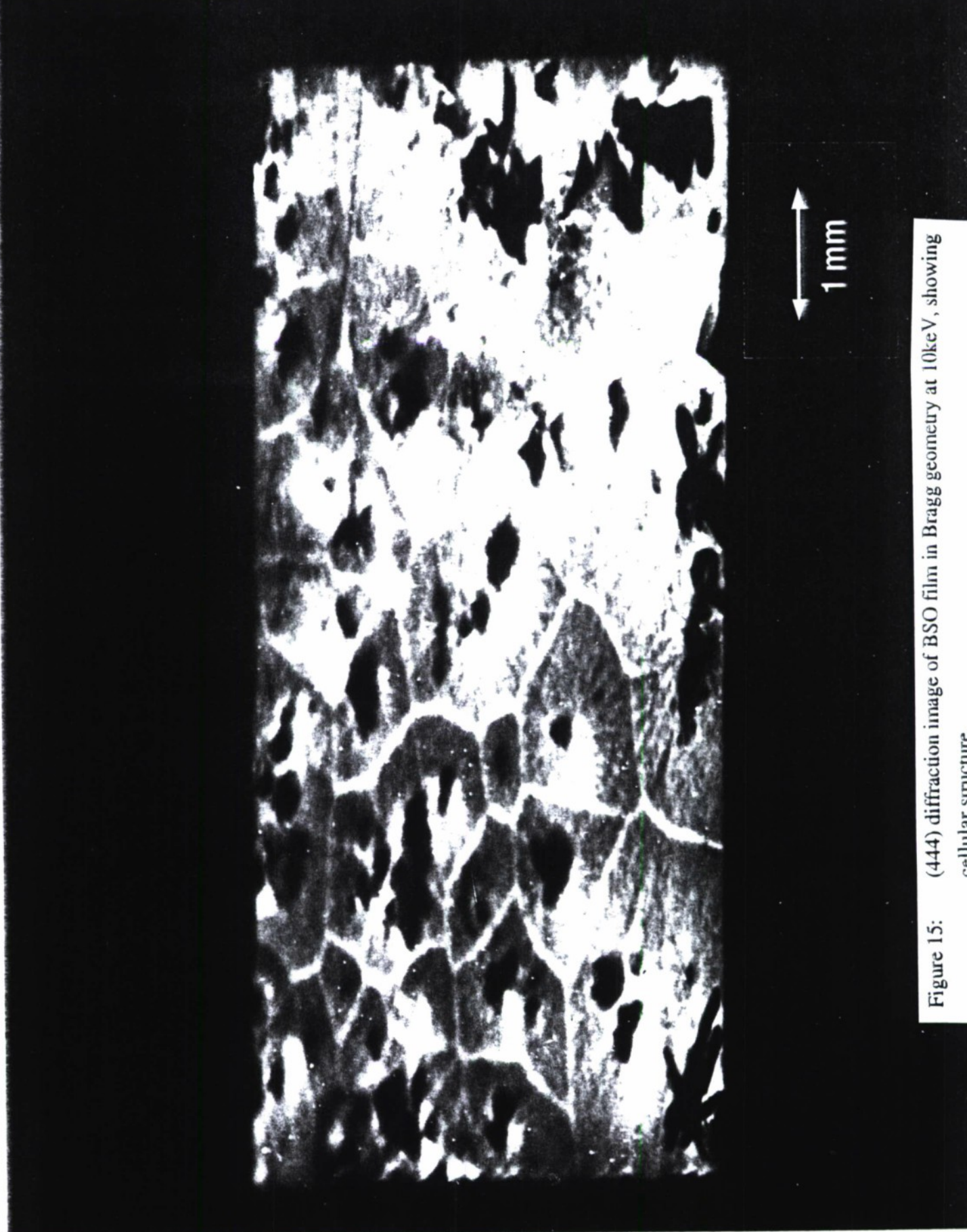


Figure 13: (800) diffraction image of SBN sample SBNSU1 in Bragg geometry at 8keV, showing surface scratches and lattice warping.



Figure 14: (004) diffraction image of SBN sample SBND1 in Bragg geometry at 8keV, showing growth striations, and odd facet shapes.



1 mm

Figure 15: (444) diffraction image of BSO film in Bragg geometry at 10keV, showing cellular structure.

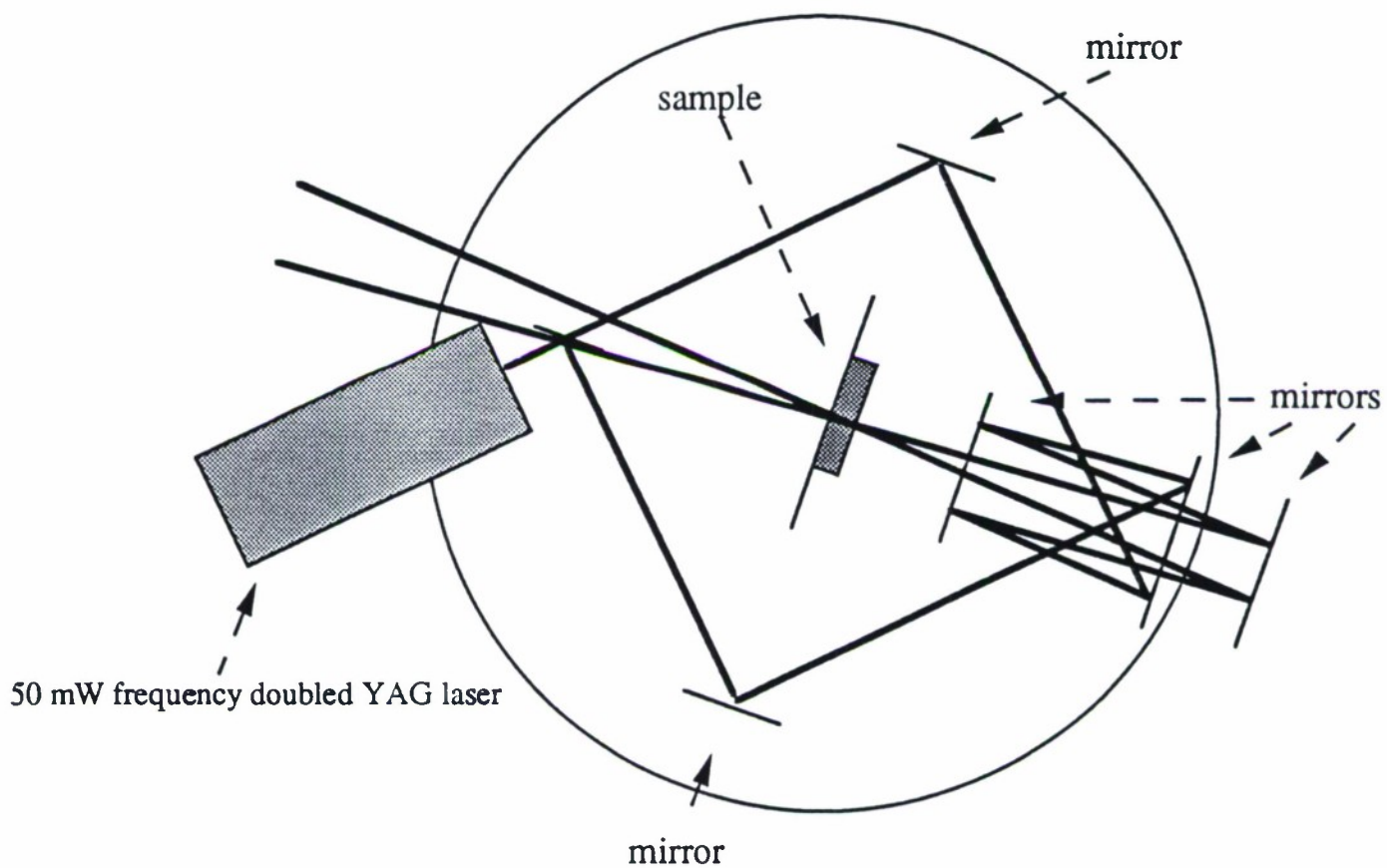


Figure 16a: Schematic of the apparatus used to write photorefractive gratings on beamline X23A3 at the National Synchrotron Light Source. The beam from the laser is split, and the two resulting beams are interfered at the crystal to produce the grating. The complicated beam path is to achieve a small angle between the beams necessary for long period ($>50\mu\text{m}$) gratings. The entire assembly rotates as a unit to allow changes in Bragg angle without altering the grating.

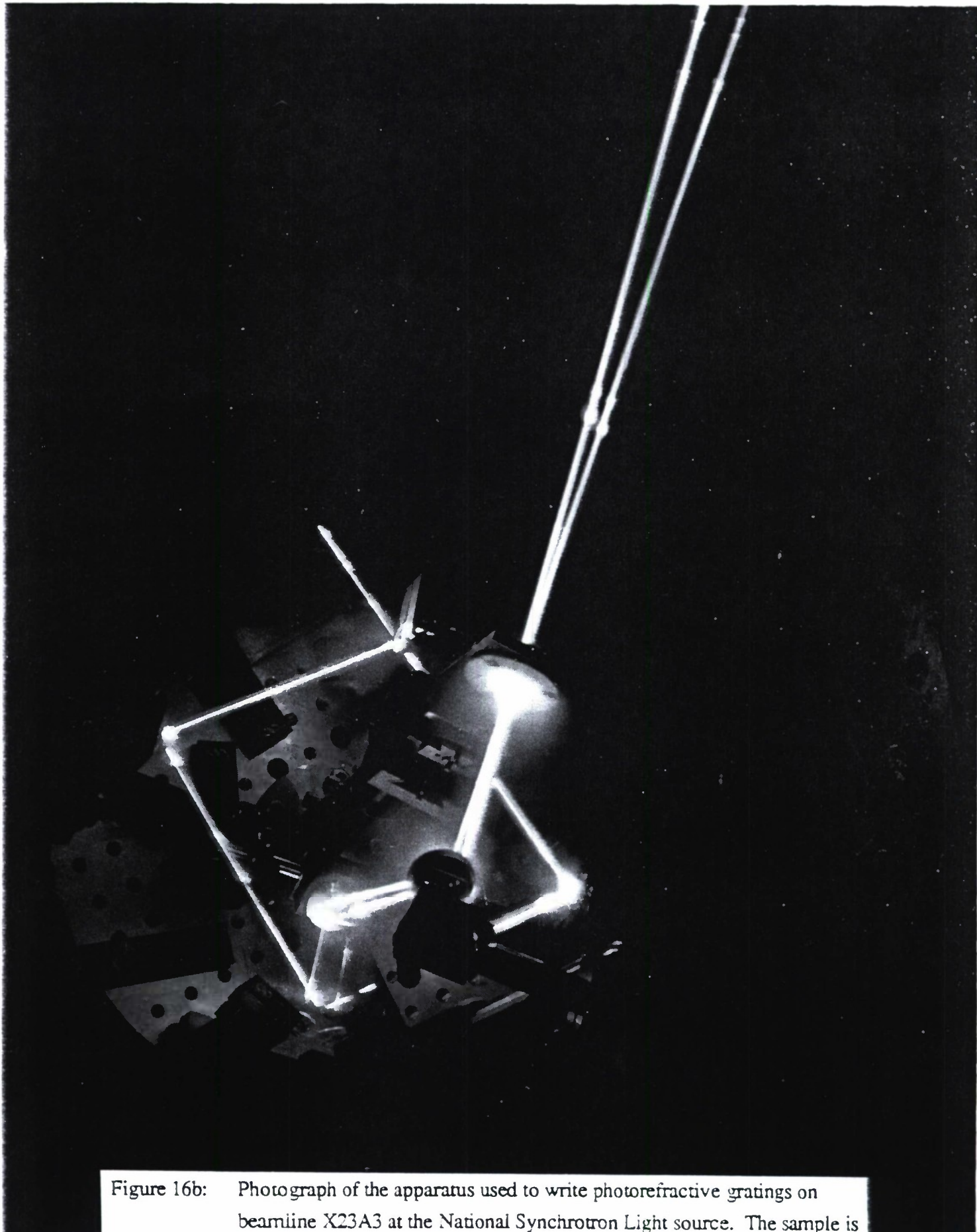


Figure 16b: Photograph of the apparatus used to write photorefractive gratings on beamline X23A3 at the National Synchrotron Light source. The sample is near the center of the photo, where the beams intersect.

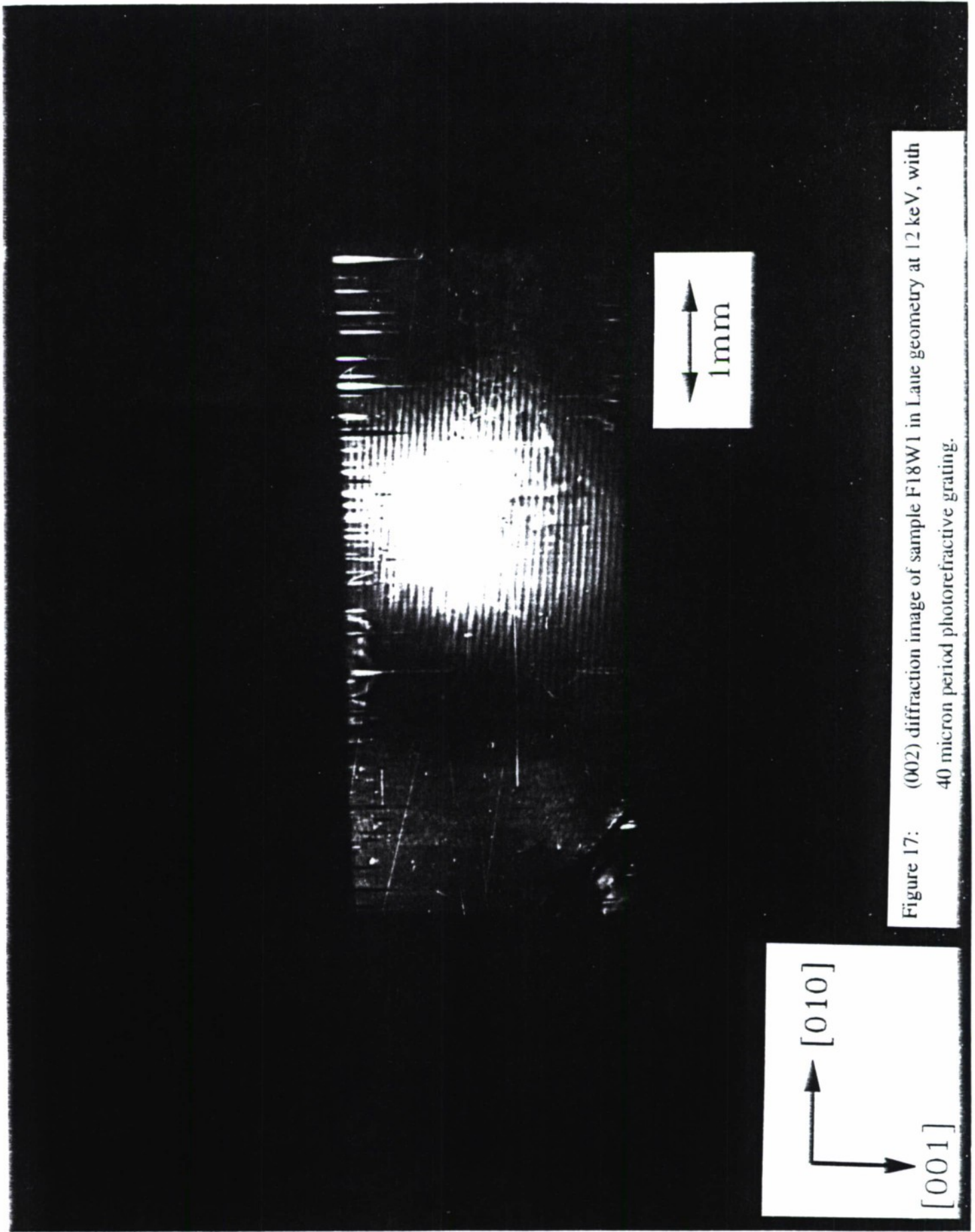


Figure 17: (002) diffraction image of sample F18W1 in Laue geometry at 12 keV, with 40 micron period photorefractive grating.

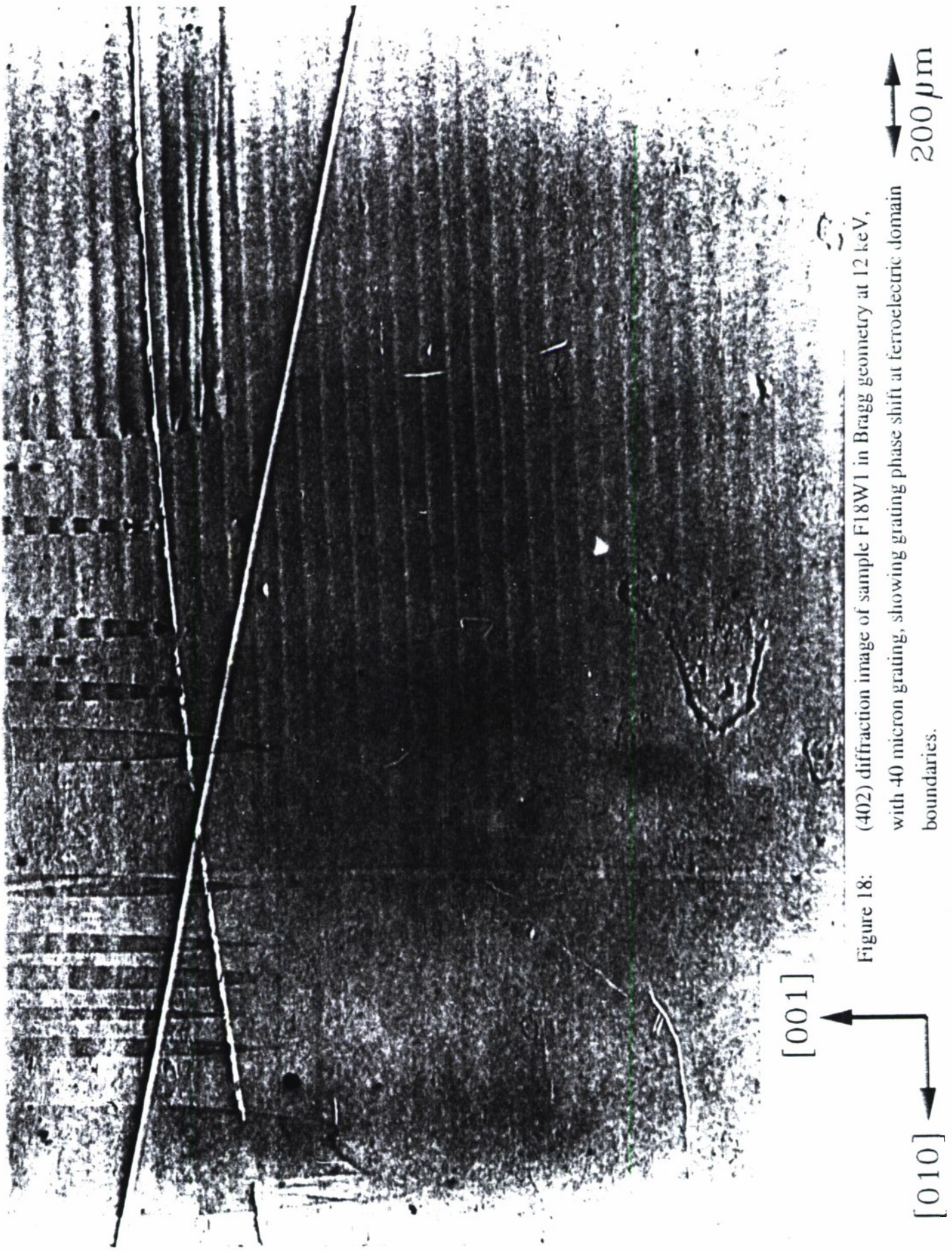


Figure 18: (402) diffraction image of sample F18W1 in Bragg geometry at 12 keV, with 40 micron grating, showing grating phase shift at ferroelectric domain boundaries.

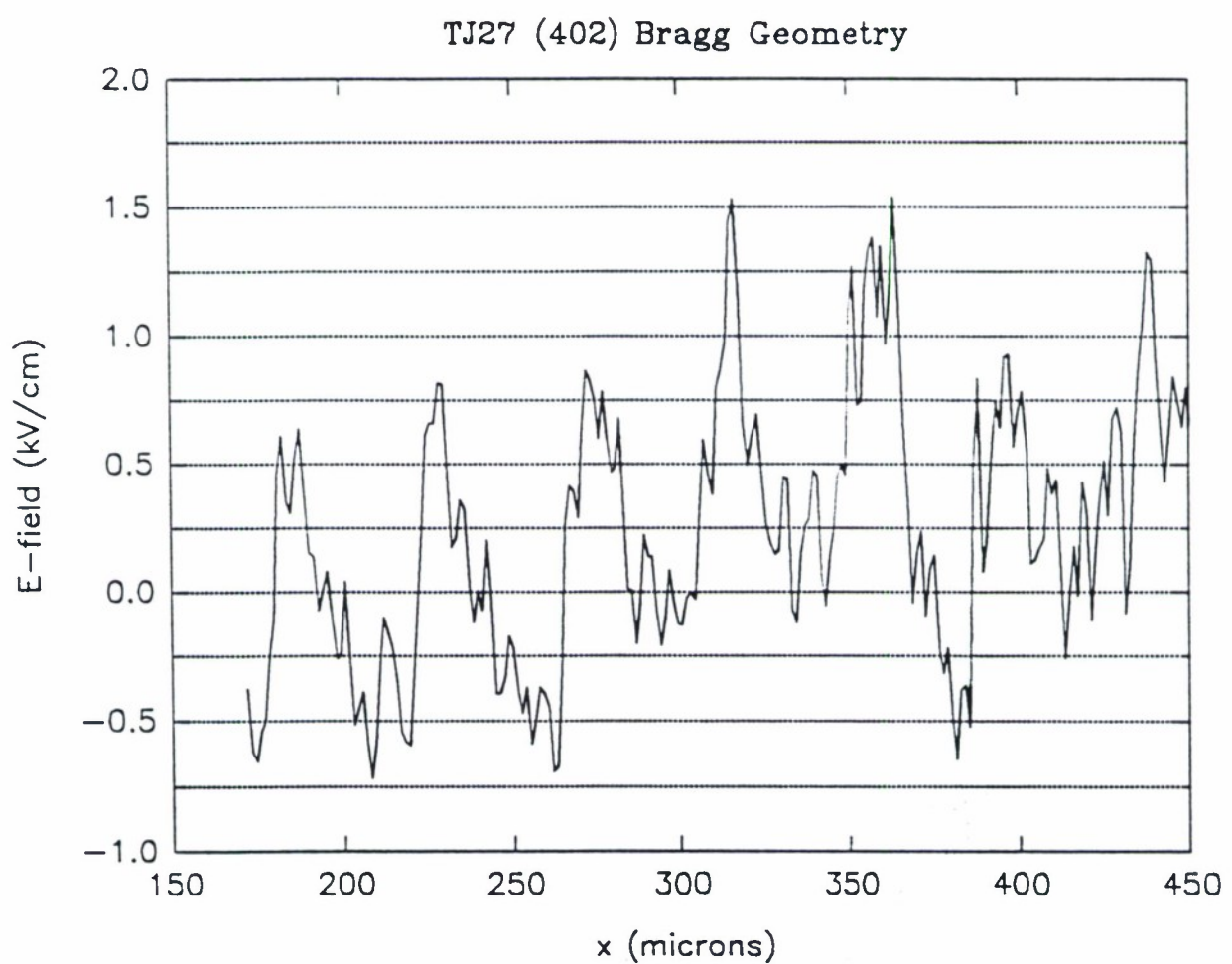


Figure 19: Photorefractive space charge field calculated from (402) Bragg geometry rocking curve sequence at 12keV.

40 Micron Grating Simulation

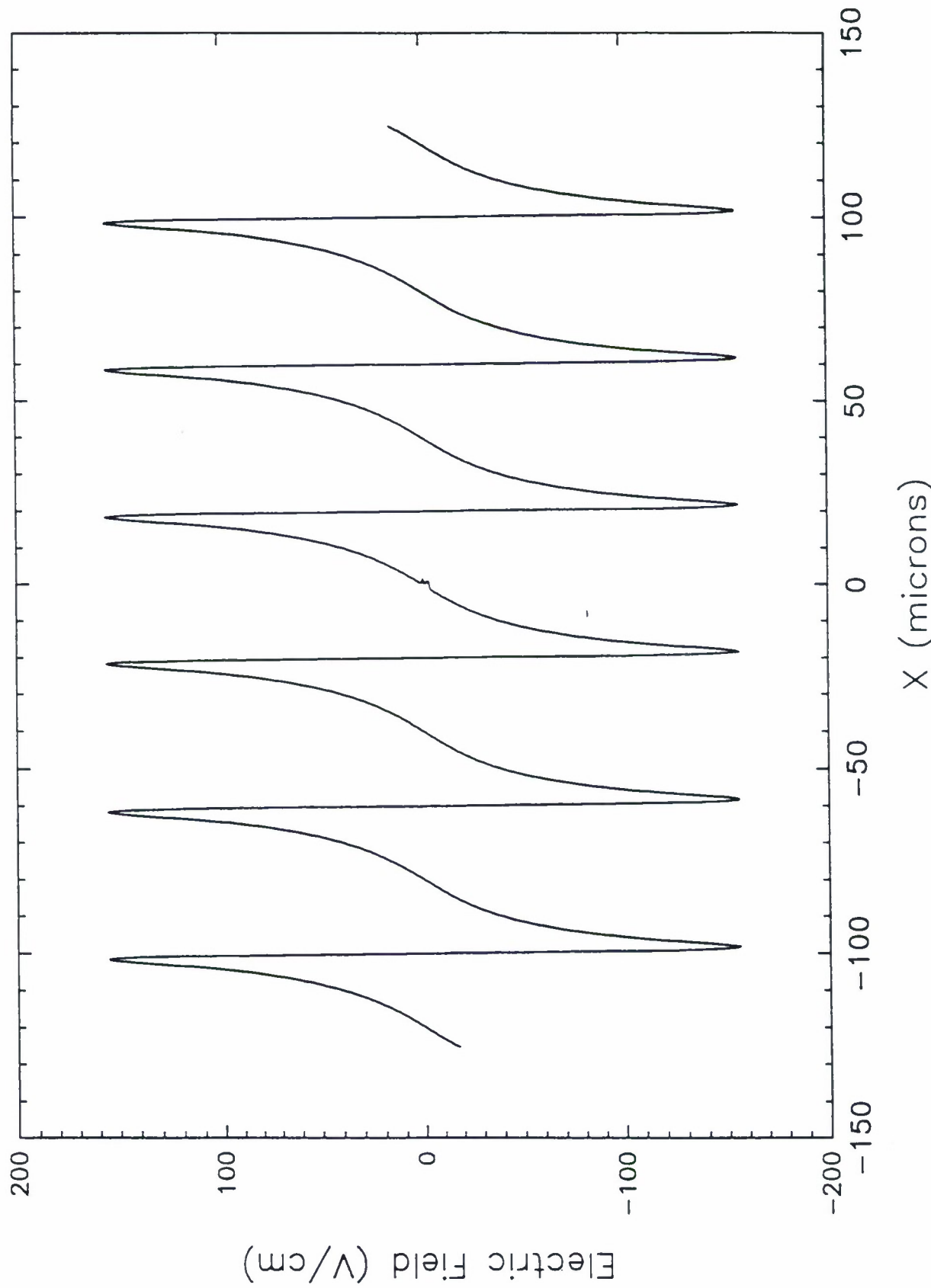


Figure 20: Simulation of the expected space charge field of 40 micron period grating in barium titanate.

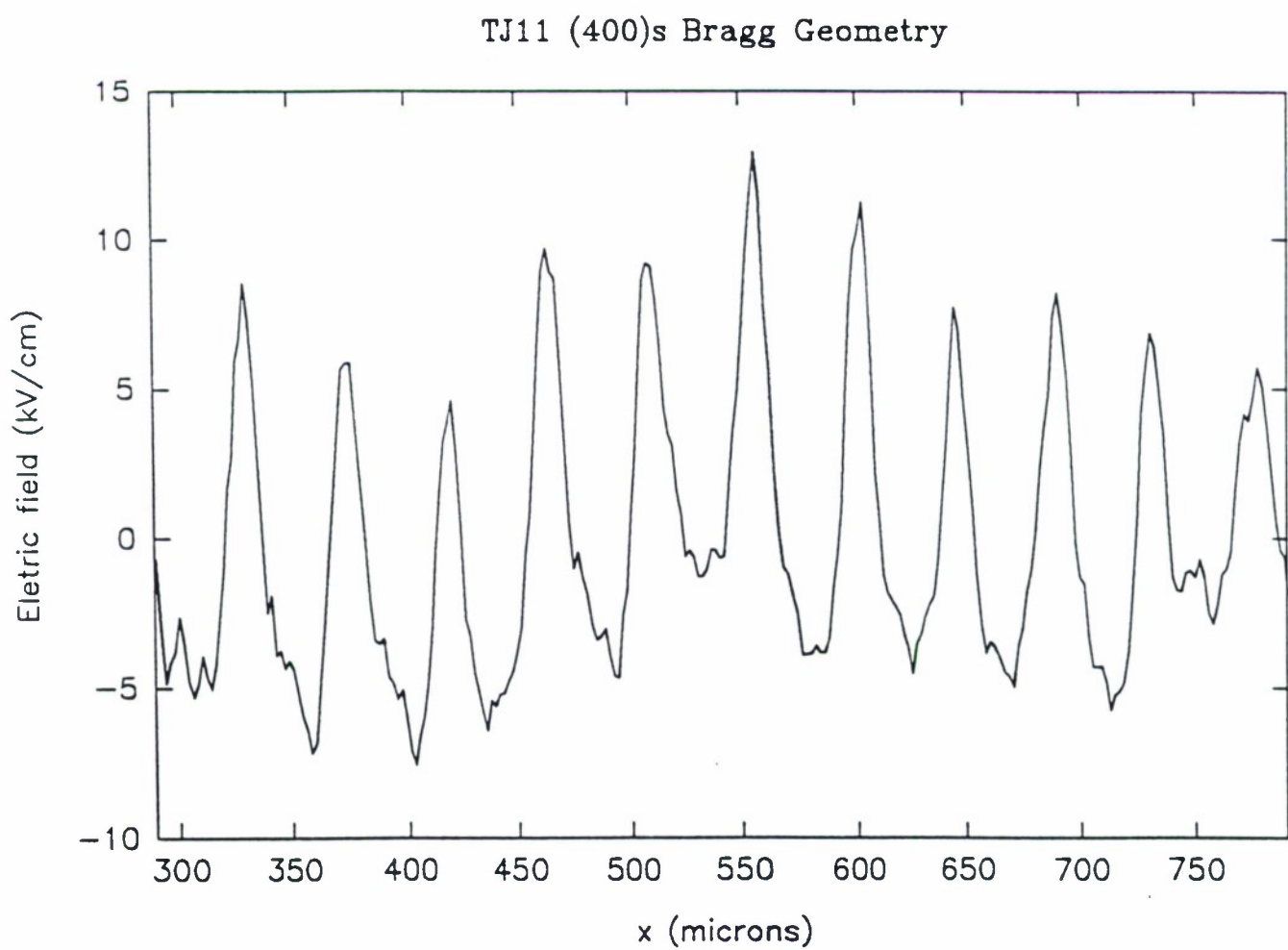


Figure 21: Photorefractive space charge field calculated from (400) Bragg geometry rocking curve sequence at 12keV.

(400) Reflection w/ Abs.

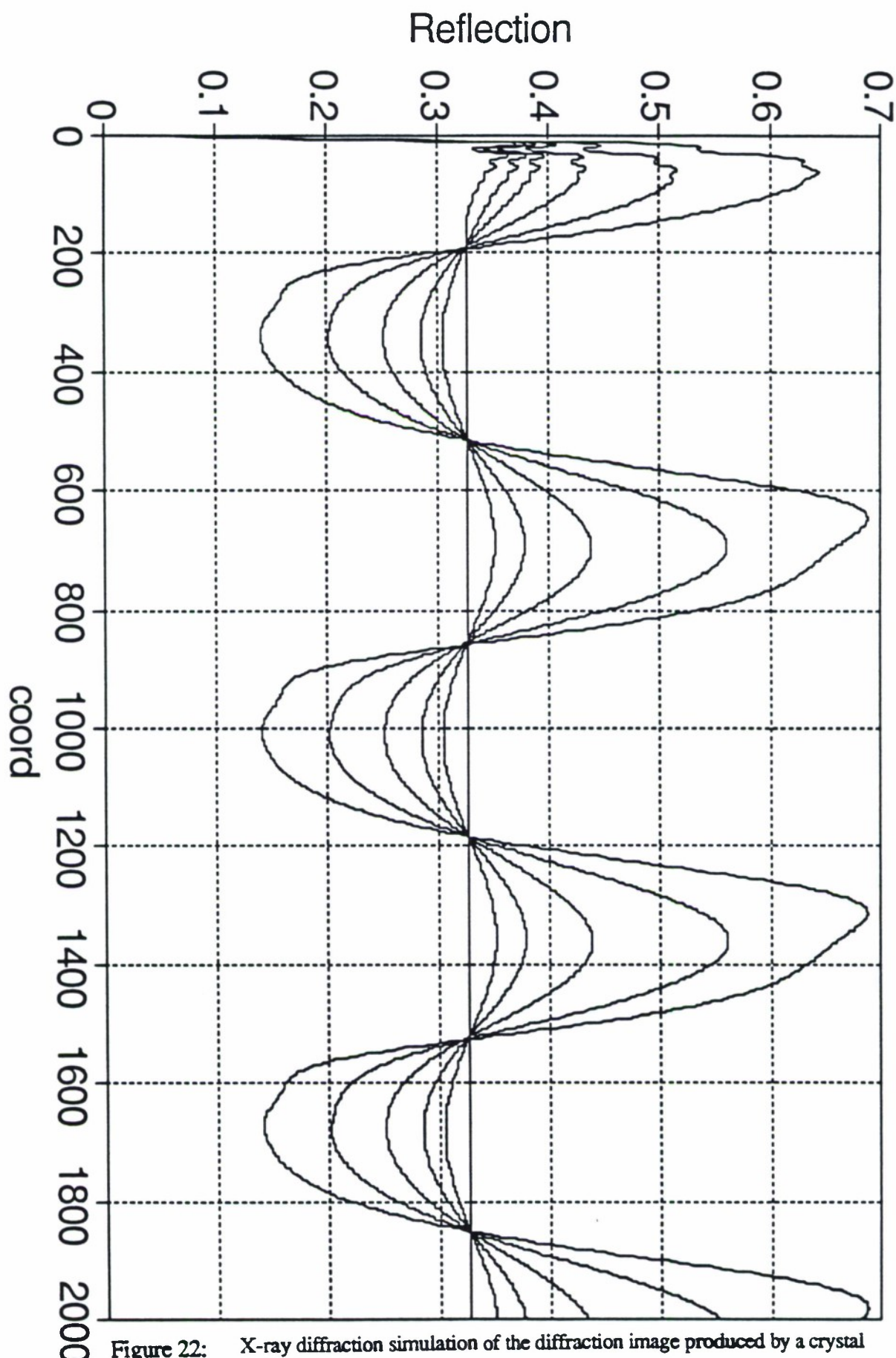


Figure 22: X-ray diffraction simulation of the diffraction image produced by a crystal with a sinusoidal grating. Successive curves represent progressively higher amplitudes of the induced sinusoidal strain, with the largest amplitude curve representing approximately the amount of strain corresponding to the grating of figure 20.



Figure 23: (002) diffraction image of sample F18W1 in Laue geometry at 12keV, showing fanning grating structure. Laser beam enters from the bottom edge of the crystal.